New filtration parameters from X-ray computed tomography for tight rock images

Paulina Krakowska-Madejska

AGH University of Science and Technology, Faculty of Geology, Geophysics and Environmental Protection, Department of Geophysics, Krakow, Poland, e-mail: krakow@agh.edu.pl, ORCID ID: 0000-0002-8261-4350

Abstract: New parameters are proposed to evaluate the filtration properties of rocks obtained on the basis of 3D interpretation of images from X-ray computed tomography. The analyzed parameters are: global average pore connectivity, average blind pore connectivity, blind pore coefficient per object and blind pore coefficient per branch. The 3D pore space from computed X-ray tomography must be subjected to a process of pore space transformation into a skeleton. Then, the presented parameters can be evaluated, taking into consideration the pore channels (branches), pore channel connection points (junctions) and blind pores (pore without connection to the other pore). The calculations were made for low porosity sandstones, mudstones, limestones, and dolomites which differ in terms of age and depth of present deposition. The global average pore connectivity reflects the degree of development of the pore space in which the formation fluid can flow. The higher the global average pore connectivity, the most complex the pore structure can be expected. The higher the parameter of the average blind pore connectivity, the worse are the filtration properties of the rock. The higher the concentration of blind pore coefficient per object or branch, the worse the filtration properties of the rock. Moreover, new parameters were compared with the Euler characteristic and coordination number, revealing a high consistency.

Keywords: new parameters for filtration properties, computed X-ray tomography, pore space, tight rocks, porosity, connectivity, pore channels

INTRODUCTION

An important aspect in exploration work is the conventional as well as unconventional approaches to interpreting the laboratory test results of rocks. One noninvasive method is computed X-ray tomography (CT), which enables the 3D analysis of pores and fractures (Arns et al. 2005, Cnudde & Boone 2013, Backeberg et al. 2017). CT images can be used for qualitative and quantitative characterization of the pores and rock filtration abilities (Soulaine et al. 2016, Lu et al. 2018), as well as for the generation of 3D geometrical models for simulation purposes, e.g., thermal or fluid flow (Krakowska & Madejski 2019, Adeleye & Akanji 2022, Al Balushi & Taleghani 2022). CT images bring new insights in the evaluation of pore size and shape. Several standard parameters can be determined based on 3D images: pore diameters, microfracture apertures, porosity, total pore area (Tsakiroglu & Payatakes 2000, Karpyn et al. 2009, Dohnalik & Jarzyna 2015). There is still scope for retrieving new information from CT images, because only one limitation is significant in CT analysis – the resolution of the measurement (Vásárhelyi et al. 2020). Below a certain resolution, which is different for different CT scanners, CT does not see pores. New

quantitative parameters describing the pore space of rocks, calculated from X-ray computed tomography (CT) results, are continually emerging in the national and global literature (Osher & Schladitz 2009). The goal of the research was connected with the discovery of new and significant parameters describing rock flow abilities. New parameters, based on the skeletonization process of the pore space from CT results, have been proposed for the assessment of rock filtration properties: global average pore connectivity (GAPC), average blind pore connectivity (ABPC), blind pore coefficient per object (BPC_object) and blind pore coefficient per branch (BPC_branch). Skeletonization process can be applied in commercial and open-source software (e.g., ImageJ). Nowadays, great importance is attached to CT image analyses as they provide valuable information on rock reservoir properties which enable effective exploitation of hydrocarbons (Golab et al. 2013, Wang et al. 2016, Liu et al. 2017, Yu et al. 2022).

METHODS

The analyses were performed on CT data for low-porosity mudstone, sandstone, dolomite, and limestone samples. The samples differ with respect to age (Cambrian, Ordovician, Silurian, Devonian, Permian), well location and burial depth (below 2000 m). In order to reduce the potential impact of CT measurement artefacts (ring artefacts) located in the center of the CT images on the calculations, each sample was divided into smaller subareas (Burliga & Dohnalik 2011) located at the corners of the sample: left upper (LG), right upper (PG), left lower (LD), right lower (PD). In the next step, only those samples were selected that were characterized by the appropriate statistics of the geometrical parameters of the pore space in the sample, including checking the correspondence of the porosity values between samples cut from a given sample.

The first step in the research was connected with the pore space transformation into a skeleton using skeletonization process on CT images. It produces an axis along each identified object in the pore space. Pores are transferred into the central axis (branches) and meet in the junctions (meeting point of pore channels). Figure 1 presents the transformation process from the 3D pore space into the network of branches (pore channels) and junctions (meeting points). All analyses on CT images were performed using the poROSE software (Technology Transfer Centre AGH University of Science and Technology in Krakow, Poland) (Krakowska et al. 2018).
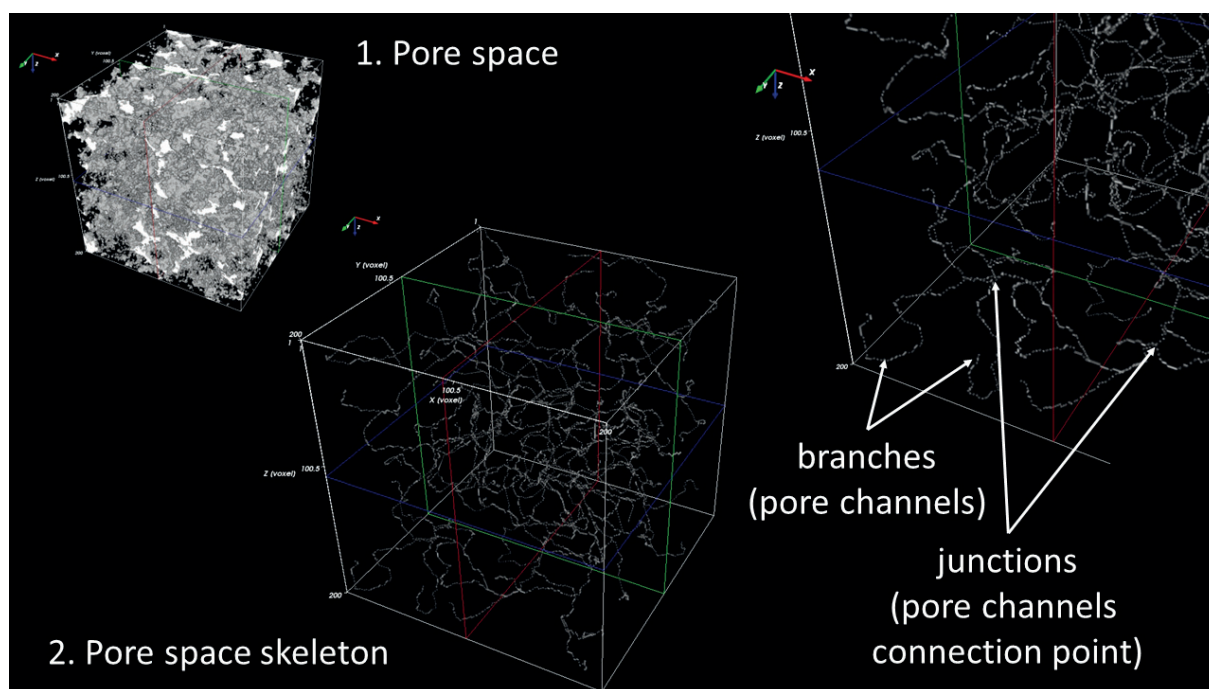

Fig. 1. *Scheme of pore space processing into pore space skeleton and skeleton elements (branches and junctions)*

The second step delivered detailed information about the blind pores (pores which do not have connections with other pores), as well as junction and number of branches. These parameters allowed the testing of the correct interpretation of the new parameters.

Laboratory X-ray computed tomography examinations were performed using a General Electric Nanotom S tomograph with a 57W X-ray tube, maximum operating voltage of 180 kV in Laboratory of Micro- and Nanotomography at AGH UST, Faculty of Physics and Applied Computer Science. In addition, a Hamamatsu HAM C 7942CA-02 detector was used. The measurement achieved a voxel size of 800×800×800 nm for each sample. A voxel is a 3D pixel. CT images were processed qualitatively and quantitatively using poROSE software (poROus materials examination SoftwarE) (Krakowska 2019). The analyses focused on the capabilities of CT in determining the geometrical parameters of the pore space. The transformation of the 3D pore space into a skeleton as well as newly developed parameters were implemented in the poROSE software.

The APC is expressed by the average number of central axis branches (skeletonized objects) that meet at a junction (Hormann et al. 2016):

$$\text{APC} = 3 \cdot \left(\frac{n_t}{n_j}\right) + 4 \cdot \left(\frac{n_q}{n_j}\right) + 5 \cdot \left(\frac{n_x}{n_j}\right) \tag{1}$$

$$\frac{n_x}{n_j} = 1 - \left(\frac{n_t}{n_j}\right) - \left(\frac{n_q}{n_j}\right) \tag{2}$$

where:

APC – average pore connectivity,
n_j – total number of junctions,
n_t – number of junctions connecting 3 branches,
n_q – number of junctions connecting 4 branches,
n_x – junctions connecting 5 or more branches.

By modifying Equation (1), it is possible to introduce and determine the GAPC and find out the average number of branches per total number of branches, i.e., the global average number of branches (post-skeletonization objects) that meet at the junction (3).

$$\text{GAPC} = 3 \cdot \left(\frac{n_t}{n_b}\right) + 4 \cdot \left(\frac{n_q}{n_b}\right) + 5 \cdot \left(\frac{n_f}{n_b}\right) + 6 \cdot \left(\frac{n_s}{n_b}\right) \tag{3}$$

where:

GAPC – global average number of branches (global average pore connectivity),
n_b – total number of branches,
n_t – number of junctions connecting 3 branches,
n_q – number of junctions connecting 4 branches,
n_f – number of junctions connecting 5 branches,
n_s – number of junctions connecting 6 branches.

The formula can also be modified by expressing the ABPC, i.e., the average number of central axis branches (post-skeletonization objects) that meet at a junction but do not connect to another junction (4):

$$\text{ABPC} = 2 \cdot \left(\frac{n_{2b}}{n_b}\right) + 3 \cdot \left(\frac{n_{3b}}{n_b}\right) + 4 \cdot \left(\frac{n_{4b}}{n_b}\right) + $$
$$+ 5 \cdot \left(\frac{n_{5b}}{n_b}\right) + 6 \cdot \left(\frac{n_{6b}}{n_b}\right) \tag{4}$$

where:
ABPC – average blind pore connectivity,
n_b – total number of branches,
n_{2b} – number of junctions connecting 2 branches which do not end in a junction (i.e. not connected to other branches),
n_{3b} – number of junctions connecting 3 branches which do not end in a junction (i.e. not connected to other branches),
n_{4b} – number of junctions connecting 4 branches that do not end in a junction,
n_{5b} – number of junctions connecting 5 branches that do not end in a junction,
n_{6b} – number of junctions connecting 6 branches that do not end in a junction.

The GAPC and the ABPC parameters provide information about the quality of the pore space network for fluid flow. The GAPC takes into consideration junctions connecting branches and the total number of branches detected in the pore space.

The more junction connecting branches, the better the connectivity of all pore space components. On the other hand, the ABPC considers junctions with blind pore channels (channels which ends at grain) and number of branches. The more junctions with blind pore channels, the worse the rock filtration abilities. Junctions connecting 3 to 5 branches were mainly observed in the analyzed rock samples, rarely connecting 6 branches. Even so, samples could be observed with 6 branches but no more. This fact led to the use of parameters for a maximum of six branches in formulas (3) and (4). The GAPC and ABPC filtration parameters refer to the average values for 3 to 6 branches meeting the junction for each object (connected pores creating one network detected as separate object, cracks) to the total number of junctions in the sample, averaging the obtained result.

The BPC_object takes the following form:

$$BPC\_object = \frac{n_{blind}}{n} \qquad (5)$$

where:

BPC_object – blind pore coefficient per object,
n_{blind} – the number of pixels at the ends of the skeleton, i.e., the blind pores in the whole sample,
n – the number of objects in the whole sample.

The BPC_branch, on the other hand, takes the following form:

$$BPC\_branch = \frac{n_{blind}}{n_b} \qquad (6)$$

where:

BPC_branch – blind pores coefficient per branch,
n_{blind} – number of pixels at the ends of the skeleton, i.e., blind pores in the whole sample,
n_b – number of skeleton branches in the whole sample.

The blind pores coefficient informs us about the filtration properties of the sample. Two samples with similar total porosity may differ in their effective porosity (i.e., pores only connected), as well as in the structure of the pore connections. The ratio defines the number of blind pores to the total number of pores (objects) or branches (pore channels). In order to perform the analyses, it is necessary to transform the pore space of a given sample into a skeleton and obtain the following information: the number of pixels at the ends of the pore channels (so-called blind pores), the total number of objects (pores) in the sample, the total number of branches in the sample (pore channels). Pore spaces with a high amount of blind pores and branches have relatively low BPC_branch and indicates a low ability of pore connectivity and thus also difficulties in fluid migration. Moreover, a high amount of blind pores and a low amount of objects means a compacted and poorly developed pore structure and the BPC_object will be relatively high. If the sample has a lot of blind pores and objects, the BPC_object is relatively low but pore space is characterized by reduced flow abilities.

An additional measurement was used in the analysis to check the reliability of new parameters. Tight rock analysis (TRA) was carried out for absolute permeability measurements and was held in the Terra Tek Schlumberger Reservoir Laboratory (Handwerger et al. 2011, Suarez-Rivera et al. 2012). The Terra Tek Laboratory applies the pulse or pressure decay method in measuring absolute permeability depending on lithology.

RESULTS

Pore space description from the computed X-ray tomography

Several parameters from CT were significant in the pore space analysis: pore volume, pore surface area, total porosity, and effective porosity (Tab. 1). Permian sample 3dls is characterized by the most extensive pore space (pore volume for 3dls_LG and 3dls_PD), with the largest volume of identified pores and cracks. Moreover, Devonian sample 4lms (4lms_PD and 4lms_LG) also shows pore space complexity in the large pore volume. Total porosity corresponds with the effective porosity and is the highest for 3dls and 4lms samples.

The relation of pore volume and effective porosity for each type of lithology is presented in Figure 2. Almost all of the analyzed samples are characterized by low effective porosity, below 10%. Only two samples (3dls and 4lms) exceed 10% in

effective porosity. Pore volume reflects total porosity because it is the sum of all detected pores and cracks in the sample. Sandstones and limestones present similar trends in relation to pore volume and effective porosity (an increase of pore volume with an increase in effective porosity). Dolomites slightly deviate from the general trend, while mudstones follow the trend.

Table 1
Pore space characterization

| Lithology	Subsample	Age	Pore volume	Surface area	Total porosity	Effective porosity
			voxels	pixels	fraction	fraction
Sandstones	1sst_LG	Cambrian	29 802 079	10 916 998	0.032	0.0059
	1sst_PD	Cambrian	31 121 522	11 297 676	0.034	0.0057
	2sst_LG	Cambrian	25 664 641	7 380 463	0.028	0.0055
	2sst_PG	Cambrian	16 504 747	4 818 097	0.018	0.0044
	3sst_LG	Ordovician	38 801 185	11 092 402	0.042	0.0110
	3sst_PG	Ordovician	37 262 911	11 096 782	0.040	0.0127
	4sst_LG	Cambrian	35 217 827	7 423 275	0.036	0.0111
	4sst_PD	Cambrian	43 400 665	8 304 052	0.044	0.0201
Mudstones	1mds_PD	Silurian	7 088 576	2 863 155	0.019	0.0007
	2mds_PD	Silurian	11 865 014	4 421 272	0.018	0.0021
	3mds_PG	Silurian	4 931 346	2 430 744	0.010	0.0002
	3mds_LD	Silurian	8 291 417	3 859 664	0.018	0.0005
Dolomites	1dls_LG	Devonian	3 231 698	799 338	0.004	0.0018
	1dls_PD	Devonian	5 712 109	1 070 200	0.008	0.0014
	2dls_LG	Permian	8 753 752	2 563 788	0.009	0.0019
	2dls_PD	Permian	10 938 338	2 911 933	0.011	0.0008
	3dls_LG	Permian	135 551 729	18 941 268	0.135	0.1152
	3dls_PD	Permian	103 743 244	14 502 067	0.103	0.0900
Limestones	1lms_LG	Devonian	26 575 087	4 147 340	0.026	0.0010
	1lms_PD	Devonian	13 792 083	2 764 341	0.014	0.0041
	2lms_LG	Ordovician	52 142 610	19 033 142	0.071	0.0332
	2lms_PD	Ordovician	41 150 733	15 062 558	0.056	0.0192
	3lms_LG	Permian	7 111 359	2 020 606	0.023	0.0025
	3lms_PD	Permian	15 326 459	4 004 206	0.050	0.0195
	4lms_LG	Devonian	50 458 898	7 468 743	0.068	0.0176
	4lms_PD	Devonian	105 675 741	14 082 551	0.142	0.1122
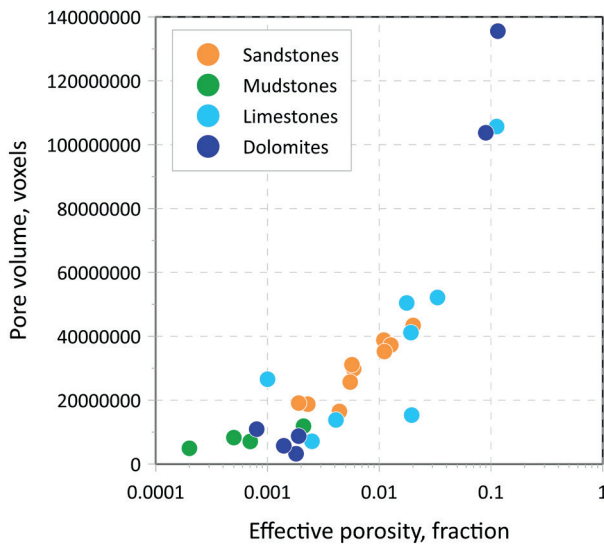
Fig. 2. *Pore volume as a function of effective porosity for different types of lithology*

Analysis of the new filtration parameters from the computed X-ray tomography

The values of the parameters: GAPC (Fig. 3) and ABPC (Fig. 4) were obtained after counting the average of the results obtained for the two subsamples, if both subsamples were available.

Otherwise, the value obtained for one subsample was included in the comparison. All types of lithology considered are shown in the comparison.

The Figures 3 and 4 indicate that the following samples: 2ss and 4ss (sandstones), 3dls (dolomite) and 2lms and 4lms (limestones) are characterized by the highest values of the GAPC and at the same time the lowest values of the ABPC. All mudstones' samples show the opposite trend, with the lowest GAPC parameter and the highest ABPC. Samples 3dls and 4lms have the highest ratio of the GAPC to ABPC parameters, 1.34 to 0.02 and 1.31 to 0.03, respectively. The average value of the GAPC and ABPC in lithological groups is 1.08 and 0.06 for sandstones, 0.43 and 0.14 for mudstones, 1.05 and 0.06 for dolomites and 1.14 and 0.06 for limestones, respectively. It is clearly visible that the lowest values are detected in mudstones and the highest in limestones for both the GAPC and the ABPC filtration parameters.

Similarly, graphs were prepared for the following parameters: the BPC_object (Fig. 5) and BPC_branch (Fig. 6).
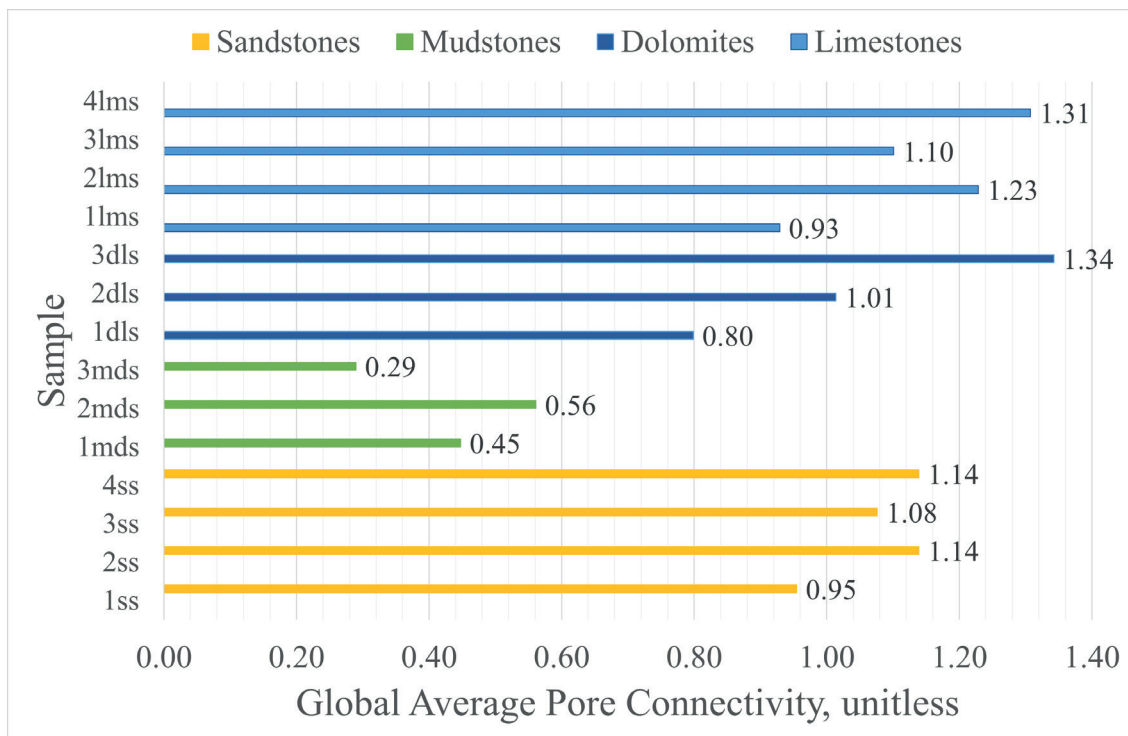

Fig. 3. *Comparison of global average pore connectivity (GAPC) values between individual samples and rock groups*
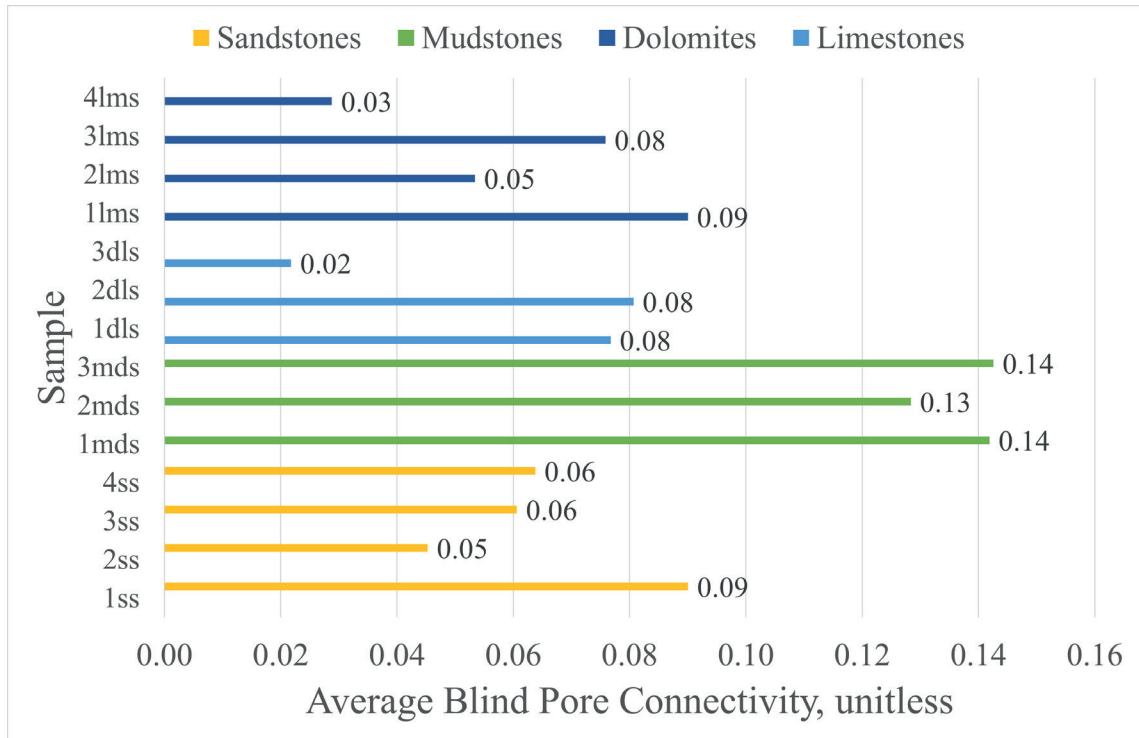
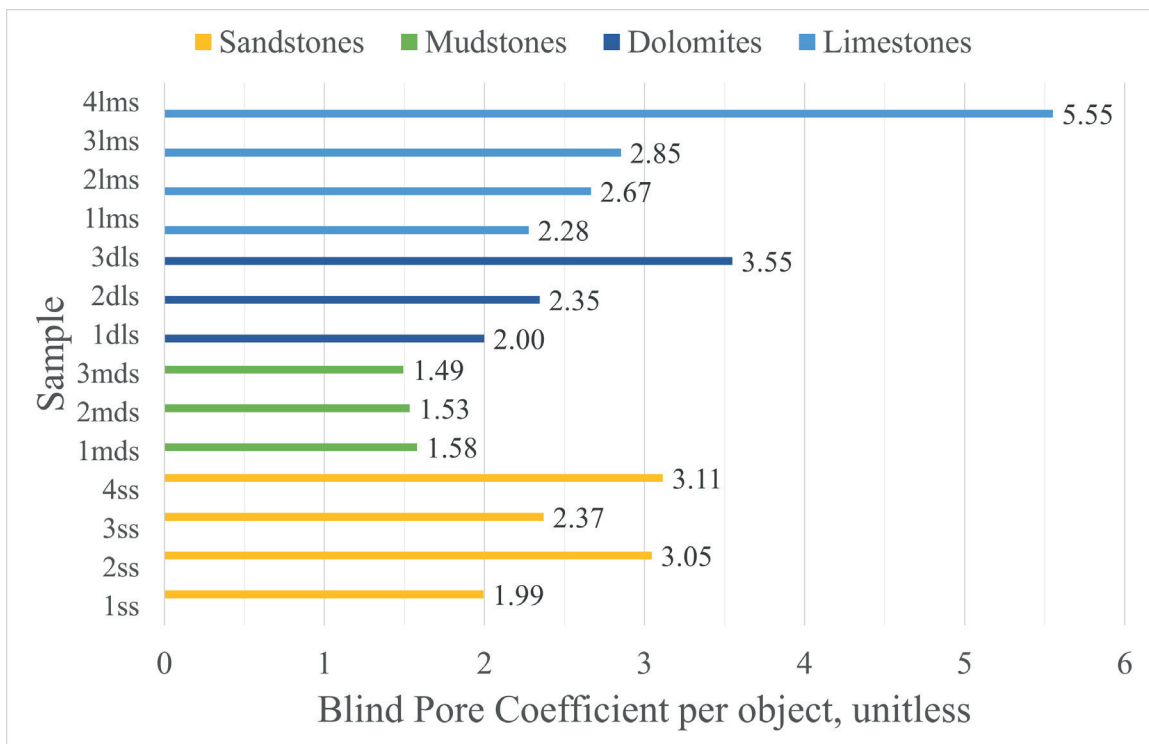**Fig. 4.** *Comparison of average blind pore connectivity (ABPC) values between individual samples and rock groups*

Fig. 5. *Comparison of blind pore coefficient per object (BPC_object) concentration values between individual samples and rock groups*
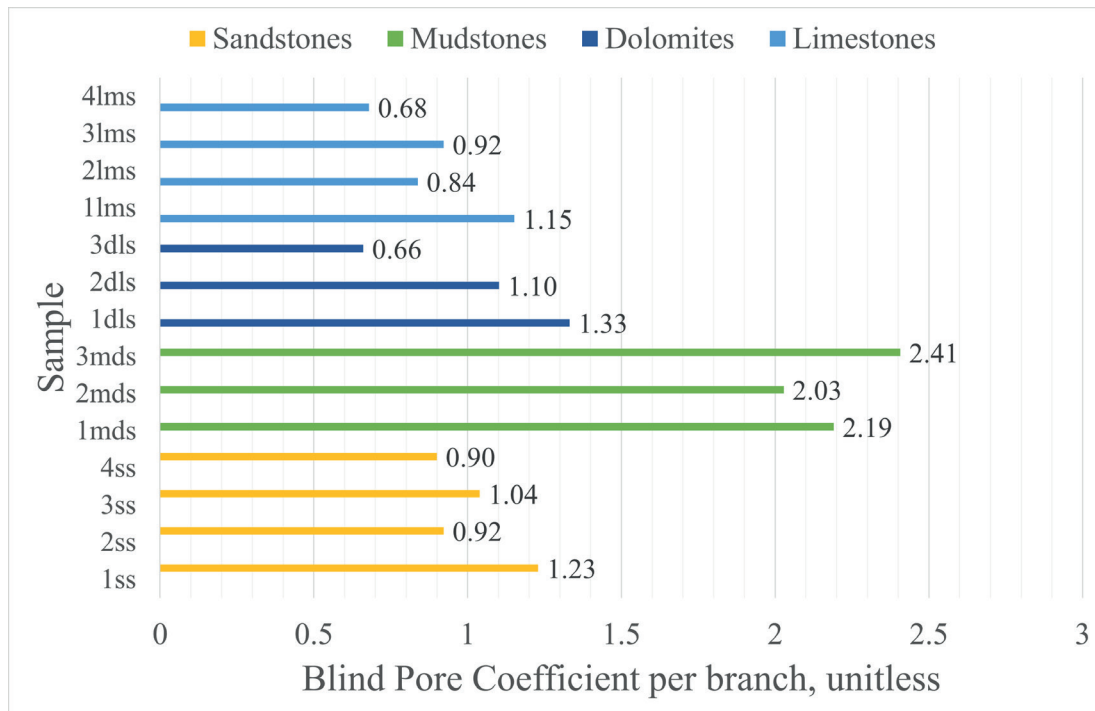
Fig. 6. *Comparison of blind pore coefficient per branch (BPC_branch) values between individual samples and rock groups*

Analysis of the BPC_object and BPC_branch parameters shows very convergent trends observed for the GAPC and ABPC filtration parameters. The mudstones samples clearly stand out from the others, having the lowest BPC_object and highest BPC_branch values. Moreover, samples 3dls and 4lms have the best ratio of the two parameters tested, respectively: 3.55 to 0.66 and 5.55 to 0.68.

Figure 7 presents relation between the GAPC and logarithm of absolute permeability (dots) and the ABPC and logarithm of absolute permeability (triangles). Colors refer to the lithology: orange – sandstones, green – mudstones, dark blue – dolomites, and light blue – limestones. It can be observed an increase in the absolute permeability with an increase in the GAPC for all lithology types. Only one sample is an outlier – sandstone with very low absolute permeability and high GAPC. Consistent trend is observed for the ABPC and logarithm of absolute permeability. The ABPC decreases with the increase in the logarithm of absolute permeability. The relation between the BPC_object and logarithm of absolute permeability and the BPC_branch and logarithm of absolute permeability is depicted in Figure 8. It

can be also noticed a decrease in the BPC_object or branch with increasing absolute permeability but not in all types of lithology. The BPC_object for carbonates did not follow the trend.
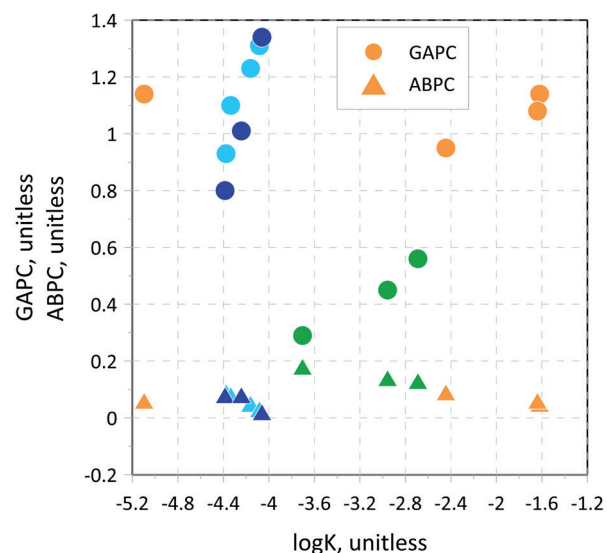

Fig. 7. *Relation between the global average pore connectivity and logarithm of absolute permeability (dots) and the average blind pore connectivity and logarithm of absolute permeability (triangles). Colors refer to the lithology: orange – sandstones, green – mudstones, dark blue – dolomites, light blue – limestones*
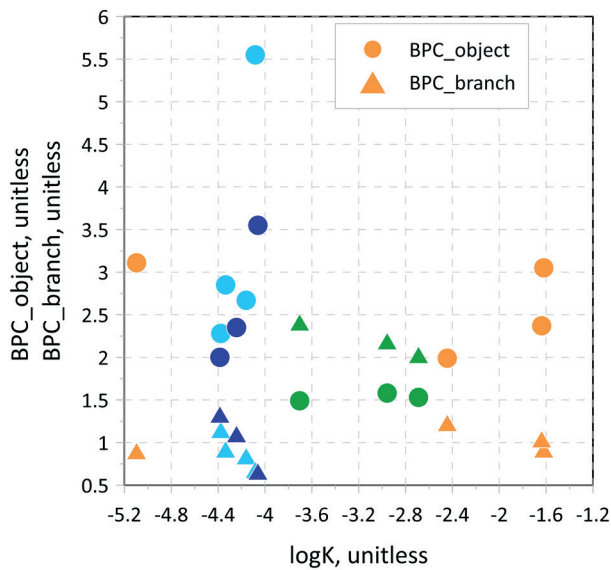
Fig. 8. Relation between the blind pore coefficient per object and logarithm of absolute permeability (dots) and the blind pore coefficient per branch and logarithm of absolute permeability (triangles). Colors refer to the lithology: orange – sandstones, green – mudstones, dark blue – dolomites, light blue – limestones

DISCUSSION

Image analysis is a powerful tool in describing rock reservoir potential. One of the first parameters connected with rock filtration abilities were presented by Toriwaki & Yonekura (2002) and Vogel (2002). They presented idea of the Euler characteristic (Euler number) in the assessment of pore structure by identifying the number of isolated pores and the number of connections (junctions) in the pore space. The formula for the Euler number is simple and is expressed by the subtraction of the number of isolated pores and the number of connections (junctions) in the pore space. Another algorithm for the Euler number, in the form of open-source code, is presented in Sossa-Azuela et al (2013). Positive values of the Euler number mean the pore structure is poorly connected, while negative values imply that the pore structure is well connected. In this case, elements of the skeletonization process can also be used in the determination of the Euler number. The GAPC, ABPC, BPC_object and BPC_branch are determined based on the elements from the pore space skeletonization process and directly

inform us about the quality of pore space connectivity. Figure 9 shows the GAPC and ABPC in comparison to Euler number. A consistent relationship between the parameters is observed. Low values of the Euler number, which indicates a well-connected pore space, corresponds with the high values of the GAPC and low values of the ABPC.
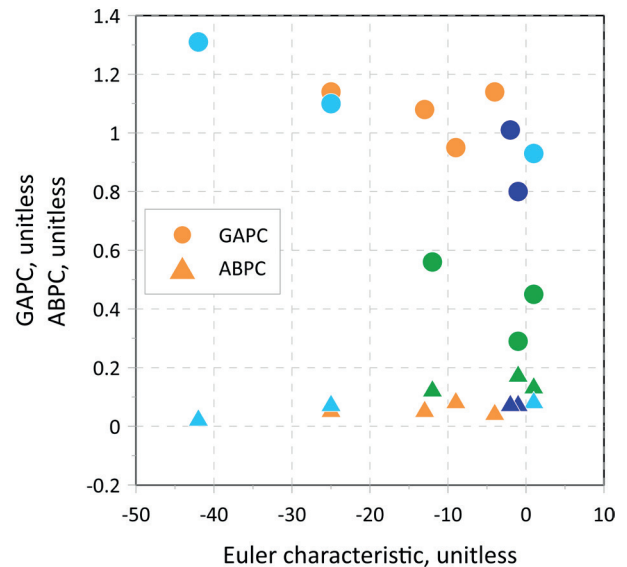

Fig. 9. Relation between the global average pore connectivity and Euler characteristic (dots) and the average blind pore connectivity and Euler characteristic (triangles). Colors refer to the lithology: orange – sandstones, green – mudstones, dark blue – dolomites, light blue – limestones

Another parameter which is important in porous material analysis is coordination number. The coordination number is defined as the number of pore channels connected to a single pore (Wayne 2008) or as the number of grains surrounding a pore (Ulusay et al. 2016). The paper by Hormann et al. (2016) also provides a definition of the pore coordination number as the number of pores connected by pore channels to the central pore. The pore channel coordination number defines the number of pores that share one pore channel. Two algorithms with formulas are presented in two papers, by Silin & Patzek (2006) and Rabbani et al. (2016). The higher the value of the coordination number, the better the filtration properties of the rock. Coordination number was

matched with the global average pore connectivity and the average blind pore connectivity (Fig. 10) for clastic rocks (sandstones and mudstones). The global average pore connectivity increases with an increase in the coordination number. On the other hand, average blind pore connectivity decreases with an increase in the coordination number. A complex pore structure with a net of well-connected pore channels is characterized by a high coordination number, as well as a high GAPC and low ABPC.
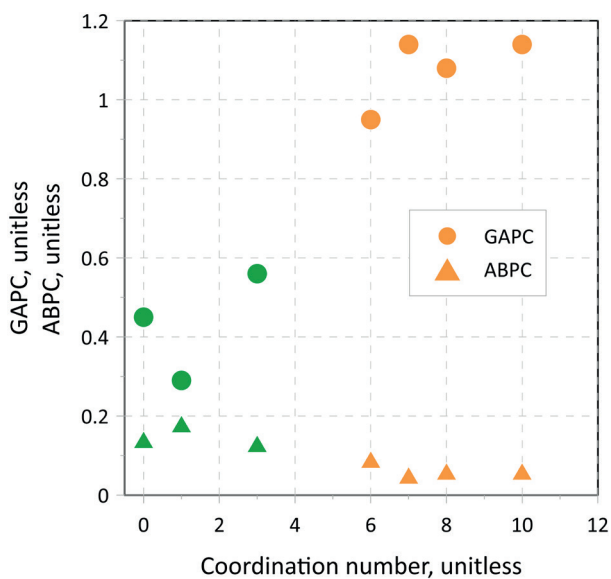

Fig. 10. *Relation between the global average pore connectivity and coordination number (dots) and the average blind pore connectivity and coordination number (triangles). Colors refer to the lithology: orange – sandstones, green – mudstones*

CONCLUSION

3D X-ray computed tomography images allow the identified pore space objects to be parameterized: pores, fractures, pore channels. The parameters developed are closely related to the filtration properties of the rock and are crucial in assessing their reservoir potential. The parameters described in this paper were implemented in the poROSE software for science and industry. The GAPC reflects the degree of pore space development in which reservoir fluid can flow without disturbances. On the one hand, the higher its value, the greater the filtration capacity of the

sample. On the other hand, the greater the parameter of the ABPC, the worse the filtration properties of the rock are in relation to the entire pore space, not just the connected pores. The knowledge of the number of connected branches and branches that are no longer connected to other branches (blind pores) can have a great impact on the assessment of the rock's capacity for hydraulic fracturing. Each fracturing treatment opens closed pores, thereby also creating a network of new pores. The blind pores may become connected, as they represent a place where the elasticity of the rock is weakened. The higher the concentration factor of the blind pores per object or branch (BPC_object, BPC_branch), the worse the filtration properties of the rock. The fluid is retained in the blind pores and is no longer able to filter the rock. New parameters were compared with the Euler number and coordination number, which are also the product of the skeletonization process of 3D pore space. Moreover, all new parameters are in consistency with the Euler number and coordination number. The potential in new filtration parameters is focused on the possibilities of assessing the rock's ability to hydraulic fracturing and thus creating new paths for fluid to flow. Computed X-ray tomography is a powerful method for describing the pore network in a three-dimensional space.

REFERENCES

Adeleye J.O. & Akanji L.T., 2022. A quantitative analysis of flow properties and heterogeneity in shale rocks using computed tomography imaging and finite-element based simulation. *Journal of Natural Gas Science and Engineering*, 106, 104742. https://doi.org/10.1016/j.jngse.2022.104742.

Al Balushi F. & Taleghani A.D., 2022. Digital rock analysis to estimate stress-sensitive rock permeabilities. *Computers and Geotechnics*, 151, 104960. https://doi.org/10.1016/j.compgeo.2022.104960.

Arns C.H., Bauget F., Ghous A., Sakellarion A., Senden T.J., Sheppard A.P., Sok R.M. et al., 2005. Digital Core Laboratory: Petrophysical analysis from 3D imaging of reservoir core fragments. *Petrophysics – The SPWLA Journal of Formation Evaluation and Reservoir Description*, 46(4), 260–277.

Backeberg N.R., Iacoviello F., Rittner M., Mitchell T.M., Jones A.P., Day R., Wheeler J. et al., 2017. Quantifying the anisotropy and tortuosity of permeable pathways in clay-rich mudstones using models based on X-ray tomography. *Scientific Reports*, 7, 14838. https://doi.org/10.1038/s41598-017-14810-1.

Burliga S. & Dohnalik M., 2011. Internal structure and origin of modern salt crust of Salar de Uyuni (Blivia) salt pan based on tomographic research. *Geology, Geophysics & Environment*, 37(2), 215–229. https://doi.org/10.7494/geol.2011.37.2.215.

Cnudde V. & Boone M.V., 2013. High-resolution X-ray computed tomography in geosciences: a review of the current technology and applications. *Earth-Science Reviews*, 123, 1–17. https://doi.org/10.1016/j.earscirev.2013.04.003.

Dohnalik M. & Jarzyna J., 2015. Determination of reservoir properties through the use of computed X-ray microtomography – eolian sandstone examples. *Geology, Geophysics & Environment*, 41(3), 223–248. https://doi.org/10.7494/geol.2015.41.3.223.

Golab A., Ward C.R., Permana A., Lennox P. & Botha P., 2013. High-resolution three-dimensional imaging of coal using microfocus X-ray computed tomography, with special reference to modes of mineral occurrence. *International Journal of Coal Geology*, 113, 97–108. https://doi.org/10.1016/j.coal.2012.04.011.

Handwerger D., Suarez-Rivera R., Vaughn K. & Keller J., 2011. *Improved petrophysical core measurements on tight shale reservoirs using retort and crushed samples*. Paper presented at the SPE Annual Technical Conference and Exhibition, Denver, Colorado, USA, October 2011, SPE-147456-MS. https://doi.org/10.2118/147456-MS.

Hormann K., Baranau V., Hlushkou D., Höltzel A. & Tallarek U., 2016. Topological analysis of non-granular, disordered porous media: determination of pore connectivity, pore coordination, and geometric tortuosity in physically reconstructed silica monoliths. *New Journal of Chemistry*, 40, 4187–4199. https://doi.org/10.1039/C5NJ02814K.

Karpyn Z.T., Alajmi A., Radaelli F., Halleck P.M. & Grader A.S., 2009. X-ray CT and hydraulic evidence for a relationship between fracture conductivity and adjacent matrix porosity. *Engineering Geology*, 103(3–4), 139–145. https://doi.org/10.1016/j.enggeo.2008.06.017.

Krakowska P., 2019. Detailed parametrization of the pore space in tight clastic rocks from Poland based on laboratory measurement results. *Acta Geophysica*, 67(6), 1765–1776. https://doi.org/10.1007/s11600-019-00331-0.

Krakowska P. & Madejski P., 2019. Research on fluid flow and permeability in low porous rock sample using laboratory and computational techniques. *Energies*, 12(24), 4684. https://doi.org/10.3390/en12244684.

Krakowska P., Puskarczyk E., Jędrychowski M., Habrat M., Madejski P. & Dohnalik M., 2018. Innovative characterization of tight sandstones from Paleozoic basins in Poland using X-ray computed tomography supported by nuclear magnetic resonance and mercury porosimetry. *Journal Petroleum Science and Engineering*, 166, 389–405. https://doi.org/10.1016/j.petrol.2018.03.052.

Liu S., Sang S., Wang G., Ma J., Wang X., Wang W., Du Y. & Wang T., 2017. FIB-SEM and X-ray CT characterization of interconnected pores in high-rank coal formed from regional metamorphism. *Journal of Petroleum Science and Engineering*, 148, 21–31. https://doi.org/10.1016/j.petrol.2016.10.006.

Lu X., Armstrong R.T. & Mostaghimi P., 2018. High-pressure X-ray imaging to interpret coal permeability. *Fuel*, 226, 573–582. https://doi.org/10.1016/j.fuel.2018.03.172.

Osher J. & Schladitz K., 2009. *3D Images of Material Structures: Processing and Analysis*. Wiley-VCH Verlag GmbH & Co. KGaA, Weinheim.

Rabbani A., Ayatollahi S., Kharrat R. & Dashti N., 2016. Estimation of 3-D pore network coordination number of rocks from watershed segmentation of a single 2-D image. *Advances in Water Resources*, 94, 264–277. https://doi.org/10.1016/j.advwatres.2016.05.020.

Silin D. & Patzek T., 2006. Pore space morphology analysis using maximal inscribed spheres. *Physica A: Statistical Mechanics and its Applications*, 371(2), 336–360. https://doi.org/10.1016/j.physa.2006.04.048.

Sossa-Azuela J.H., Santiago-Montero R., Perez-Cisneros M. & Rubio-Espino E., 2013. Computing the Euler number of a binary image based on a vertex codification. *Journal of Applied Research and Technology*, 11(3), 360–370. https:// doi.org/10.1016/S1665-6423(13)71546-3.

Soulaine C., Gjetvaj F., Garing C., Roman S., Russian A., Gouze P. & Tchelepi H.A., 2016. The impact of sub-resolution porosity of X-ray microtomography images on the permeability. *Transport of Porous Media*, 113, 227–243. https://doi.org/10.1007/s11242-016-0690-2.

Suarez-Rivera R., Chertov M., Willberg D., Green S. & Keller J., 2012. *Understanding permeability measurements in tight shales promotes enhanced determination of reservoir quality*. Paper presented at the SPE Canadian Unconventional Resources Conference, Calgary, Alberta, Canada, October 2012, SPE-162816-MS. https://doi.org/10.2118/162816-MS.

Toriwaki J. & Yonekura T., 2002. Euler number and connectivity indexes of a three dimensional digital picture. *Forma*, 17, 183–209.

Tsakiroglu Ch.D. & Payatakes A.C., 2000. Characterization of the pore structure of reservoir rocks with the aid of serial sectioning analysis, mercury porosimetry and network simulation. *Advances in Water Resources*, 23(7), 773–789. https://doi.org/10.1016/S0309-1708(00)00002-6.

Ulusay R., Aydan O., Gerçek H., Ali Hindistan M. & Tuncay E., 2016. *Rock Mechanics and Rock Engineering: From the Past to the Future*. CRC Press, Taylor & Francis Group, London.

Vásárhelyi L., Kónya Z., Kukovecz A. & Vajtai R., 2020. Microcomputed tomography-based characterization of advanced materials: a review. *Materials Today Advances*, 8, 100084. https://doi.org/10.1016/j.mtadv.2020.100084.

Vogel H.-J., 2002. Topological Characterization of Porous Media. [in:] Mecke K. & Stoyan D. (eds.), *Morphology of Condensed Matter: Physics and Geometry of Spatially Complex Systems*, Lecture Notes in Physics, 600, Springer, Berlin, Heidelberg, 75–92.

Wang J., Zhao J., Zhang Y., Wang D., Li Y. & Song Y., 2016. Analysis of the effect of particle size on permeability in hydrate-bearing porous media using pore network models combined with CT. *Fuel*, 163, 34–40. https://doi.org/10.1016/j.fuel.2015.09.044.

Wayne M.A., 2008. *Geology of Carbonate Reservoirs: The Identification, Description, and Characterization of Hydrocarbon Reservoirs in Carbonate Rocks*. Willey & Sons Inc., Hoboken.

Yu X., Butler S.K., Kong L., Mibeck B., Barajas-Olalde C., Burton-Kelly M.E. & Azzolina N.A., 2022. Machine learning-assisted upscaling analysis of reservoir rock core properties based on micro-computed tomography imagery. *Journal of Petroleum Science and Engineering*, 219, 11108. https://doi.org/10.1016/j.petrol.2022.111087.